

AD

TECHNICAL REPORT ARCCB-TR-96003

**SELF-ORGANIZED CRITICAL BEHAVIOR IN A DOMAIN
WALL DYNAMICS MODEL DESCRIBING BARKHAUSEN EFFECT**

L. V. MEISEL

JANUARY 1996



**US ARMY ARMAMENT RESEARCH,
DEVELOPMENT AND ENGINEERING CENTER
CLOSE COMBAT ARMAMENTS CENTER
BENÉT LABORATORIES
WATERVLIET, N.Y. 12189-4050**



APPROVED FOR PUBLIC RELEASE; DISTRIBUTION UNLIMITED

19960501 161

DTIC QUALITY INSPECTED 1

DISCLAIMER

The findings in this report are not to be construed as an official Department of the Army position unless so designated by other authorized documents.

The use of trade name(s) and/or manufacturer(s) does not constitute an official indorsement or approval.

DESTRUCTION NOTICE

For classified documents, follow the procedures in DoD 5200.22-M, Industrial Security Manual, Section II-19 or DoD 5200.1-R, Information Security Program Regulation, Chapter IX.

For unclassified, limited documents, destroy by any method that will prevent disclosure of contents or reconstruction of the document.

For unclassified, unlimited documents, destroy when the report is no longer needed. Do not return it to the originator.

REPORT DOCUMENTATION PAGE

Form Approved
OMB No. 0704-0188

Public reporting burden for this collection of information is estimated to average 1 hour per response, including the time for reviewing instructions, searching existing data sources, gathering and maintaining the data needed, and completing and reviewing the collection of information. Send comments regarding this burden estimate or any other aspect of this collection of information, including suggestions for reducing this burden, to Washington Headquarters Services, Directorate for Information Operations and Reports, 1215 Jefferson Davis Highway, Suite 1204, Arlington, VA 22202-4302, and to the Office of Management and Budget, Paperwork Reduction Project (0704-0188), Washington, DC 20503.

1. AGENCY USE ONLY (Leave blank)		2. REPORT DATE January 1996		3. REPORT TYPE AND DATES COVERED Final	
4. TITLE AND SUBTITLE SELF-ORGANIZED CRITICAL BEHAVIOR IN A DOMAIN WALL DYNAMICS MODEL DESCRIBING BARKHAUSEN EFFECT				5. FUNDING NUMBERS AMCMS No. 6111.02.H611.1	
6. AUTHOR(S) L.V. Meisel					
7. PERFORMING ORGANIZATION NAME(S) AND ADDRESS(ES) U.S. Army ARDEC Benet Laboratories, AMSTA-AR-CCB-O Watervliet, NY 12189-4050				8. PERFORMING ORGANIZATION REPORT NUMBER ARCCB-TR-96003	
9. SPONSORING / MONITORING AGENCY NAME(S) AND ADDRESS(ES) U.S. Army ARDEC Close Combat Armaments Center Picatinny Arsenal, NJ 07806-5000				10. SPONSORING / MONITORING AGENCY REPORT NUMBER	
11. SUPPLEMENTARY NOTES Submitted to <i>Physical Review E</i> .					
12a. DISTRIBUTION / AVAILABILITY STATEMENT Approved for public release; distribution unlimited.				12b. DISTRIBUTION CODE	
13. ABSTRACT (Maximum 200 words) A simple domain wall dynamical model, incorporating a normal distribution of pinning strengths on a simple cubic lattice of pinning sites, a nearest neighbor elastic interaction, and demagnetization effects with a simple dynamical rule, yields a succession of fractal scaling structures as the applied field is increased. Furthermore, each domain wall configuration in the succession supports size effect cutoff power law distributions of avalanches (i.e., Barkhausen noise pulses) when perturbed. The size effect parameters correlate with the ranges of fractal scaling.					
14. SUBJECT TERMS Self-Ordered Critical Systems, Barkhausen Effect, Ferromagnetism				15. NUMBER OF PAGES 26	
				16. PRICE CODE	
17. SECURITY CLASSIFICATION OF REPORT UNCLASSIFIED	18. SECURITY CLASSIFICATION OF THIS PAGE UNCLASSIFIED	19. SECURITY CLASSIFICATION OF ABSTRACT UNCLASSIFIED	20. LIMITATION OF ABSTRACT UL		

TABLE OF CONTENTS

	<u>Page</u>
ACKNOWLEDGEMENTS	iii
INTRODUCTION	1
THE DOMAIN WALL DYNAMICAL MODEL	2
Forces	2
Dynamics	3
NUMERICAL STUDIES	4
Evolution of Domain Wall Structure	4
Avalanche Statistics and Barkhausen Noise	4
Spatial Scaling and Fractal Analysis	5
RESULTS	6
DISCUSSION	9
CONCLUSION	10
REFERENCES	12

TABLES

1. Summary of Fitting Parameters Derived From the Data of Figures 3 Through 9 14

LIST OF ILLUSTRATIONS

1. Internal field versus applied field on 65x65 lattices 15
2. Internal field versus applied field and fractal dimension versus applied field
for the {100,10,4000} model on a 65x65 lattice 16
3. A selection of results for the {100,1,1000} model for $H = 200$ on a 129x129 lattice .. 17
4. A selection of results for the {100,1,1000} model for $H = 500$ on a 129x129 lattice .. 18

5.	A selection of results for the $\{100,1,1000\}$ model for $H = 700$ on a 129×129 lattice . .	19
6.	A selection of results for the $\{100,1,1000\}$ model for $H = 1000$ on a 129×129 lattice .	20
7.	A selection of results for the $\{100,1,1000\}$ model for $H = 1500$ on a 129×129 lattice .	21
8.	A selection of results for the $\{100,1,1000\}$ model for $H = 1000$ on a 1025 linear lattice	22
9.	A selection of results for the $\{100,1,1000\}$ model for $H = 1500$ on a 1025 linear lattice	23

ACKNOWLEDGEMENTS

The author is pleased to acknowledge helpful discussions with A. Abbate, P.J. Cote, and M. A. Johnson.

INTRODUCTION

Bak et al. (ref 1) introduced the concept of self-organized criticality (SOC) to provide a consistent explanation for the fractal spatial structures, power law distributions, and flicker noise commonly observed in spatially-extended, dissipative, dynamical systems. The consequences of the SOC concept have been extensively explored through computer simulations of sandpile dynamics (refs 1-4) and analysis of earthquake phenomena (refs 5,6).

The most dramatic application of SOC concepts pertains to the earth's crust. The state of the earth's crust, a complex dissipative dynamical system, is thought of as a self-organized critical system so that the Gutenberg-Richter law for the distribution of earthquake magnitudes (ref 5) is seen as a natural consequence of the SOC nature of the system. There is also a growing body of experimental investigations of SOC-related phenomena including studies of actual sandpile dynamics (refs 7,8), motion of magnetic domains in garnet films (ref 9), and sliding friction (ref 10). The stochastic character of domain wall jumps arises from the complex patterns of local magnetic fields, internal stresses, and bulk and surface defects (pinning sites) in ferromagnetic alloys. References 11 through 13 demonstrate that the Barkhausen effect is an excellent candidate for SOC description.

The response of ferromagnets to applied magnetic fields is determined by the distribution of pinning sites, the initial magnetic domain distribution, and the domain wall dynamics. For small fields, kinetic barriers permit small reversible domain wall motions and the system remains magnetically elastic in analogy with elastic-plastic deformation or slip-stick SOC earthquake models (ref 5). As the applied field increases, the domain walls are able to break free of the weaker pinning sites and domain wall motion commences. As the applied field increases further, more extensive domain wall excursions occur. For large enough applied fields, the coercive force is exceeded and the specimen magnetization increases rapidly. The transition region is characterized by random clusters of irreversible domain wall jumps (avalanches) analogous to slip in solids when the applied force exceeds the yield strength and produces rapid, step-like increases in strain.

Recently, Urbach et al. (ref 13) demonstrated that a domain wall dynamical model incorporating demagnetization effects could lead to exponentially cutoff power law distributions of avalanches near critical states over a wide range of parameter values. These were important results. However, Urbach et al. did not establish the fractal nature of the scaling of the domain wall structures, nor did they describe the distribution of avalanches in the subcritical ($H < H_c$) or supercritical ($H > H_c$) driving field cases.

In this report the behavior of the Urbach et al. model (ref 13) is examined in more detail. It is demonstrated that the "self-organization" process passes through a sequence of states, each one of which

1. Yields cutoff power law distributions of avalanche sizes if perturbed, and
2. Exhibits fractal scaling over a range of scales.

Items 1 and 2 are fingerprints of SOC phenomena and it is interesting that they are exhibited for subcritical and supercritical, as well as critical, driving fields for the Urbach et al. model (ref 13).

Since References 2 and 12 demonstrate that cutoff power law distributions of the avalanche distribution give rise to flicker noise in the power spectral density, time-scale invariance (flicker noise) over increasing time scales and length-scale invariance (fractal scaling) over increasing spatial scales develop as the model is driven through a sequence of self-organized states. Furthermore, the range of fractal scaling correlates with the size effect parameters in the cutoff power law fits, and at the critical driving field H_c , fractal scaling may be observed over essentially all scales for the two-dimensional domain wall models studied. The one-dimensional domain wall models behave like the two-dimensional models except that fractal scaling over all scales is not observed for $H \geq H_c$.

THE DOMAIN WALL DYNAMICAL MODEL

The domain wall model employed in this study and its origins have been discussed by Urbach et al. (ref 13). Its form can be traced back to fundamental ideas: Langevin equations, Markov processes, etc. (refs 14-26). However, it may also be seen as the simplest model incorporating domain wall rigidity, a prescribed distribution of domain wall pinning strengths, and demagnetization effects. The model has the following elements:

Forces

Domain Wall Pinning Forces

Pinning sites are assumed to be located on a simple cubic lattice. The pinning force on the lattice sites is usually taken to be normally distributed with zero mean. The pinning force on site $\{i, j, k\}$ is denoted $u(i, j, k)$. The variance σ of the distribution is a parameter in the model, which essentially determines the scale for the applied field H . The effects of assuming that the pinning forces are normally distributed about a binding value are also discussed briefly.

Driving Forces

The domain wall is driven by an applied field H , which produces an internal field h . The internal field h in the presence of demagnetizing effects is assumed to be given in terms of the applied field H as

$$h = H - \eta M \quad (1)$$

where η is the demagnetization factor and the effective magnetization M is taken as the mean deflection of the domain wall, i.e.,

$$M = \langle z \rangle = \frac{1}{L} \sum_{i=1}^L \frac{1}{N} \sum_{j=1}^N z(i, j) \quad (2)$$

where the sums run over undeflected domain wall sites (which lie in a principal plane of the pinning site lattice) and $z(i, j)$ is the deflection at the i, j position. H , h , and ηM are expressed in units of force on the domain wall. The introduction of a demagnetizing field as in Eq. (2) was shown to have important consequences in Reference 13. The quantity η is a parameter in the model.

Elastic Coupling

A simple form of elastic restoring force based only on nearest neighbor deflection differences is assumed. The elastic constant k is assumed to be homogeneous and isotropic and is a parameter in the model. Combining the three types of forces yields

$$f(i, j, z(i, j)) = h + u(i, j, z(i, j)) + k(z(i+1, j) + z(i-1, j) + z(i, j+1) + z(i, j-1) - 4z(i, j)) \quad (3)$$

for the net force $f(i, j, z(i, j))$ on the domain wall site at position $\{i, j, z(i, j)\}$, where the elastic coupling is described by the k -multiplied term in Eq. (3). On the edges of the model spaces, the missing deflections are taken to be equal to the deflection at the reflected lattice site. For example, the deflection at $i, j = (L+1)$, is taken to be $z(i, L-1)$ in Eq. (3). Essentially the same results were obtained by replacing the 4-nearest neighbor form of Eq. (3), by a 3-nearest neighbor form on an edge, etc.

Dynamics

At each time step, every domain wall site $\{i, j, z(i, j)\}$ for which the net force is positive, i.e., $f(i, j, z(i, j)) > 0$, advances one step, i.e., $z(i, j) \rightarrow z(i, j) + 1$.

In practice, one does not maintain a three-dimensional array of pinning strength values. At each step to a new value of $z(i, j)$, one selects at random a new value of $u(i, j, z(i, j))$ from the assumed distribution of pinning strengths.

NUMERICAL STUDIES

Evolution of Domain Wall Structure

The domain wall structures described in this work were obtained by beginning with a planar domain wall, $z(i, j) = 0$, with either a normal distribution of pinning forces or $u(i, j, 0) = 0$. (Results were essentially indistinguishable for $H \geq 200$ in the present model studies.) The driving field was then increased in small increments with respect to the "critical fields" allowing the domain wall to move until all forces are negative. The structure as described by its fractal scaling was not substantially changed by cutting the steps in half in the cases for which results are reported.

Avalanche Statistics and Barkhausen Noise

We define the SIZE of an avalanche as the number of lattice sites traversed by a domain wall in an avalanche. The distribution of avalanche sizes obtained by sequentially perturbing single lattice pinning sites in a static (self-organized) domain wall configuration produced by the evolution of domain wall structure was determined as follows:

1. A domain wall site is chosen at random.
2. The pinning strength at the selected site is reset to a new value from the normal distribution of pinning strengths.
3. If the site becomes unstable,
 - a. The ensuing avalanche is allowed to go (at fixed H) until all forces are negative.
 - b. The SIZE of the avalanche is stored.
 - c. After the avalanche is completed, the $z(i, j)$ and $u(i, j)$ are reset to their original values.

If the site does not become unstable, the $u(i, j)$ is returned to its original value. Steps 1 through 3 are repeated until the desired number of avalanches has been produced.

Essentially the same avalanche distributions were obtained in tests in which the *force* at the randomly selected site was set positive. Also note that even though the same sites are traversed by many avalanches, the pinning strengths in the lattice through which the avalanches propagate are different each time.

Spatial Scaling and Fractal Analysis

The domain dynamical model under investigation yields a single valued domain wall deflection $z(i, j)$. It is, therefore, possible to define a hierarchy of approximations of the domain wall surface in terms of triangles of different sizes in an unambiguous way. The extent of the lattice models studied has been adjusted to facilitate the triangular approximations. Taking

$$L = N = 2^n + 1 \text{ for integer } n$$

in Eq. (2) enables one to define sets of triangles whose vertices coincide with subsets of points on the domain wall and whose projections in the xy-plane are right triangles of side lengths, which we refer to as "yardsticks Y" given by

$$Y(m) = 2^m \text{ for } m = \{0, 1, \dots, n\}$$

Clearly, all of the triangles for the m^{th} approximation have areas

$$A_i(m) \geq Y(m)^2/2$$

Although no attempt is made to adjust the triangular approximations to obtain extremal areas (which would be required in a rigorous algorithm for the fractal dimension) for a given class of triangles, the small $Y(m)$ approximations to fractal surfaces will scale approximately according to

$$\lim_{m \rightarrow 0} \frac{d \ln(A(m))}{d \ln(Y(m))} = 2 - D \quad (4)$$

where the area $A(m)$ corresponding to the m^{th} approximation is taken as the sum of the individual triangle areas

$$A(m) \equiv \sum_i A_i(m)$$

and D is a fractal dimension. Note that the smallest yardstick in the set is $Y(0) = 1$, which is as far as one can go in the analysis of a surface defined on a discrete lattice of points.

The reliability of the algorithm has been tested with Euclidean and "Brown" surfaces (ref 27). Brown constructions were selected for the tests because elevations are single valued, as required by the algorithm, and because D can be adjusted to have any value between 2 and 3. The measured area

$$\lim_{m \rightarrow 0} A(m) = \text{True Area}$$

and $D = 2.0$ was returned for Euclidean surfaces. The Mandelbrot fractal dimension for 65x65 Brown constructions was given within 2.5 percent for $D = 2.1$, within 1.5 percent for $D = 2.2$, and within 0.5 percent for $2.9 \geq D \geq 2.3$ by the algorithm. The Mandelbrot fractal dimension for 129x129 Brown constructions was given within 2.5 percent for $D = 2.1$, within 1.0 percent for $D = 2.2$, within 0.5 percent for $D = 2.3$, and within 0.2 percent for $2.9 \geq D \geq 2.4$ by the algorithm.

To determine the fractal dimensions for the one-dimensional domain wall models, piecewise linear approximations (where the x-axis projection of each segment has length $Y(m)$, etc.) replace the triangular approximations.

All calculations were performed in **MATLAB**TM.

RESULTS

Figure 1 displays graphs of internal field h versus applied field H for models having parameters $\{k = 100, \eta = 1, \sigma = 1000\}$, $\{k = 100, \eta = 3, \sigma = 1000\}$, $\{k = 100, \eta = 10, \sigma = 1000\}$, and $\{k = 100, \eta = 1, \sigma = 2000\}$ on a 65x65 lattice. The $k = 100, \sigma = 1000$ curves saturate at $H = H_c \approx h \approx 0.8\sigma$. As η increases, the break becomes less sharp; for $\eta = 10$, there is no sharp transition at all. The $k = 100, \eta = 1, \sigma = 2000$ curve saturates for $H \approx h \approx 1.2\sigma$. The transition point generally increases with increasing σ . Similar curves were obtained for 33x33, 129x129, and 257x257 lattices.

Figure 2 shows fractal dimension D versus applied field H and internal field H versus H curves for a $k = 100, \eta = 1, \sigma = 4000$ model on a 65x65 lattice, which saturates at $H = H_c \approx 6000$. The fractal dimension of the self-organized domain wall structures increases with H to approximately 2.75 at $H \approx 1500$; D is then approximately independent of H until $H \approx 4000$; as H increases beyond 4000, D decreases smoothly to about 2.3 at $H \approx 6000$. The D values measured for $H > 6000$ are scattered between about 2.25 and 2.35. Except for the actual magnitudes, the graphs of Figures 1 and 2 are typical of results for the two-dimensional domain wall models studied.

One also finds generally that the variations in the fractal dimension D with H passing through the critical region become weaker as η increases and the value of D and its variation with H passing through the critical region becomes stronger as σ increases. Furthermore, the influence of the k parameter in these models can be inferred from the variations with σ : one finds that a system defined by parameters $\{k, \eta, \sigma\}$ on a 129x129 lattice, which assumes a

self-organized state at a driving field H behaves like a system defined by parameters $\{k/2, \eta, \sigma/2\}$ on a 65×65 lattice at a driving field of $H/2$ in the sense that the fractal dimensions are essentially the same and the cutoff parameters scale appropriately.

Figures 3 through 7 display results obtained for the $\{k = 100, \eta = 1, \sigma = 1000\}$ model on a 129×129 lattice for a selection of values of the driving field H . The critical field $H_c \approx 1000$ for this model. Figures 3 and 4 present subcritical results, $H = 200$ and 500 , "substantially below" H_c . Figure 5 exhibits results obtained for $H = 700$; the dramatic changes evident in the lower panels indicate that one is entering the critical region. Figure 6 exhibits results for $H = 1000 \approx H_c$. Figure 7 presents supercritical results, $H = 1500 > H_c$. Avalanche statistics are based on 10,000 events in all cases shown.

Each figure in the set has four parts.

1. The upper left-hand subplot shows a contour map of the domain wall displacements. A 65×65 section of the domain wall is shown for $H \leq 700$; the full 129×129 contour map is shown for $H \geq 1000$. There are five equally spaced contour levels in all cases.
2. Plots of $\log_2(A(m)/A(7))$ versus $\log_2(Y(m)/Y(7))$ and the small yardstick fits are given in the upper right-hand graphs.
3. The lower left-hand subplots show the distribution of avalanche sizes in logarithmically-spaced bins and the results of one or two least squares fits. The straight lines are least squares fit to the smaller size half of the distributions; the curves are least squares fit to the form

$$y = C(1)x^{-C(2)} \exp(-x/C(3)) \quad (5)$$

using the **MATLAB**TM function `fmins`, which is a realization of the Nelder Mead Simplex Algorithm (ref 28). We refer to the straight line fits as "sharp cutoff" fits and to curves of the form in Eq. (5) as "exponentially cutoff" fits. The author is not aware of any theoretical basis for choosing one form over the other. In some cases sharp cutoff fits provide a better description of the data, in some cases exponentially cutoff fits are better, and in other cases either functional form seems to describe the data equally well. One should note that even in the exponentially cutoff fits, there is an implicit sharp cutoff, since one does not attempt to include the next (unoccupied, $N = 0$) bin in the fitting.

4. The lower right-hand subplots show the distribution of avalanche sizes in linearly-spaced bins and the results of a least squares fit to Eq. (5) employing `fmins` (ref 28). In some cases the least squares fits are weighted with $\ln(N)^2$ in order to force the fit curves to more closely approximate the first bin occupation. The x values plotted and used in the least squares fits are taken at the center of mass rather than the centers of the bins. The linearly-spaced bin distributions fit Eq. (5) better than a sharp cutoff form in every case.

Figure 3 gives results for $H = 200$. The contour plot illustrates the cell-like substructure, which obtains for H substantially less than H_c . The fractal scaling extends out to yardsticks of about 2^2 and is consistent with $D \approx 2.49$. The log-binned avalanche statistics fit both the sharp cutoff or the exponentially cutoff forms reasonably well. The linear-binned results fit Eq. (5) well also. The denominators in the exponential cutoffs are of the order of the area of the largest triangles in the scaling range (i.e., $(2^2)^2 = 16$).

Figure 4 gives results for $H = 500$. The contour plot again exhibits cell-like substructure, however the cells are larger than those observed in the $H = 200$ case. The fractal scaling extends out to yardsticks of about 2^3 and is consistent with $D \approx 2.52$. The log-binned avalanche statistics fit both the sharp cutoff and the exponentially cutoff forms well. The linear-binned results fit Eq. (5) also. The denominators in the exponential cutoffs are of the order of the area of the largest triangles in the scaling range (i.e., $(2^3)^2 = 64$).

Figure 5 gives results for $H = 700$. The cell-like substructure is larger scale than the $H = 500$ case. The fractal scaling extends out to yardsticks of about 2^5 and is consistent with $D \approx 2.40$. The log-binned avalanche statistics fit both the sharp cutoff and the exponentially cutoff forms reasonably well. The linear-binned results fit Eq. (5) well. The denominator in the exponential cutoff is of the order of the area of the largest triangles in the scaling range (i.e., $(2^5)^2 = 1024$). The reduction of the fractal dimension and the appearance of substantially larger avalanches are indications that H is entering the transition region in the class of domain wall models studied. The jump in the $C(3)$ parameter determined by the least squares fit to Eq. (5) and the estimated "sharp cutoff" value provide additional quantitative indications that H is entering the critical region.

Figure 6 gives results for $H = 1000$. The domain wall structure is now on the scale of the entire construction. The fractal scaling extends out to yardsticks of about 2^7 and is consistent with $D \approx 2.30$. This is the critical case. The log-binned avalanche statistics fit both the sharp cutoff and the exponentially cutoff forms reasonably well. The linear-binned results fit Eq. (5); however, almost all the events correspond to the smallest avalanche bin; the denominator in the exponential cutoff is of the order of the area of the largest triangles in the scaling range (i.e., $(2^7)^2 = 16,384$), which corresponds to the full spatial extent of the model. The sharp cutoff also approximates $(2^7)^2$.

Figure 7 exhibits results for $H = 1500$. The domain wall structure is again on the scale of the entire construction. Although there are small deviations from perfect scaling for some of the larger yardsticks, the fractal scaling extends out to yardsticks of about 2^7 and is consistent with $D \approx 2.30$. The log-binned avalanche statistics fit the sharp cutoff form well, but the fit to Eq. (5) degenerates to a pure power law form. The linear-binned results fit Eq. (5), almost all the events correspond to the smallest avalanche bin, and the exponential and sharp cutoff values are of the order of the full spatial extent of the model.

Essentially the same sequence of fractal structures and parameter values is obtained for a $\{k = 100, \eta = 1, \sigma = 1000\}$ model on a 65×65 lattice, except that the maximum scaling range only extends to 2^6 and maximal cutoffs correspond more closely to $64^2 (= 4096)$. Less systematic results for $\{k = 100, \eta = 1, \sigma = 1000\}$ models on 33×33 and 257×257 lattices are consistent with those on the 65×65 and 129×129 lattices. Similar sequences were obtained for all two-dimensional $\{k, \eta, \sigma\}$ models studied.

The effect of taking the pinning distribution normally distributed about a negative (binding) mean is to make the buildup of the fractal dimension of the domain wall more gradual. However, once the driving force H exceeds the "binding force" by δH , the fractal structures become indistinguishable from those occurring for $H = \delta H$ in the case that the pinning distribution has zero mean.

The one-dimensional domain wall models studied exhibited similar trends, except for the fractal scaling at $H \geq H_c$. Figure 8 shows results for $\{k = 100, \eta = 1, \sigma = 1000\}$ model on a length 1025 one-dimensional lattice ($H_c \approx 1500$) for $H = 1000$. The upper left-hand figure now shows a length 100 section of the domain wall deflections. The fractal scaling extends out to yardsticks of about 2^5 and is consistent with $D \approx 1.37$. The log-binned avalanche statistics fit the sharp cutoff form and Eq. (5) reasonably well. The linear-binned results fit Eq. (5) and the exponential and sharp cutoff values are of the order of 2^5 .

Figure 9 shows results for the same model for $H = 1500 \approx H_c$. The spatial scaling is now more complex. There is a region of approximate fractal scaling ($D = 1.13$) for yardsticks ranging from 1 to 2^4 and a second region of approximate fractal scaling ($D = 1.59$) for yardsticks ranging from 2^4 to 2^7 . The log-binned avalanche statistics fit the sharp cutoff form and Eq. (5) reasonably well. The linear-binned results fit Eq. (5). The exponential and sharp cutoff values are of the order of the full spatial extent of the model rather than 2^7 .

The one-dimensional models yield results consistent with the two-dimensional models for $H < H_c$. However, the $H \geq H_c$ results generally split into two scaling regions as in Figure 9 for the one-dimensional models. At larger values of H , the small yardstick scaling range is essentially unchanged and the large yardstick scaling range becomes larger with D values near 1.60 for the $\{100, 1, 1000\}$ model on a 1025 length lattice. The avalanche distributions are generally consistent with a cutoff hyperbolic form as observed in Reference 13 for the one-dimensional domain wall models studied.

The fitting parameters deduced from the data in Figures 3 through 9 are given in Table 1.

DISCUSSION

The size effect parameters $C(3)$ correlate with the scaling range of the fractal structures and with the cell structure apparent in contour plots of the domain wall configurations for $H < H_c$ and with the geometrical size/dimensions of the models for $H \geq H_c$.

As had been observed for $H \approx H_c$ in Reference 13, the one- and two-dimensional domain wall models yield linear-binned exponential size effect cutoff power law avalanche distributions for all $H > H_c/5$. However, as observed in References 11 and 12, in many practical cases almost all avalanches fall into the shortest avalanche linear-spaced bin and as shown, for example, in Figure 2 of Reference 13, the probability of the longest avalanche detected is frequently of the order of 10^{-4} times as large as the probability of observing a short avalanche. Thus, in order to represent the avalanche distribution for linearly-spaced binning correctly, one needs to detect rare events very accurately.

In the event the smallest avalanche bin dominates the distribution in linearly-binned cases, the data are also consistent with a sharp cutoff pure power law form for logarithmically-binned data. Thus, it is a good idea to keep open the option of employing logarithmic sharp cutoff fitting in cases of experimental data where the form of the linearly-spaced bin distribution is dominated by low probability events.

The parameters reported in Table 1 can be compared to the measured sharp cutoff log-binned values of M reported for Barkhausen effect in Reference 12, where values of $-M$ ranged from 0.58 to 1.1, and to the value of $C(2)$ measured as 1.33 for linearly-spaced bins in Reference 13. The models do not reproduce the larger values of $-M$ observed in Reference 12 for the range of $\{k, \sigma, \eta\}$ explored here; however, it is clear that the value of $C(2)$ (viz., 1.29), which results from the present two-dimensional domain wall model for $H = 700$ (and is approximately the point at which the transition to critical behavior begins), is in good agreement with the value measured in Reference 13.

The splitting into two separate scaling regions for $H \geq H_c$ in the one-dimensional domain wall models is interesting, but may not be observable.

CONCLUSION

The principal result of the present study is that domain wall dynamical models incorporating

- A normal distribution of pinning strengths on a simple cubic lattice of pinning sites,
- Only nearest neighbor elastic interactions, and
- A simple description of demagnetization effects

that are governed by a simple dynamical rule give rise to domain wall configurations, which evolve through a hierarchy of fractal structures, which are scale-invariant over increasing ranges of scales as the driving field H increases toward and through a critical value H_c , and which at all

stages of development yield size effect cutoff hyperbolic (power law) distributions of avalanches (Barkhausen noise) when perturbed. Size effects are determined by physical dimensions for $H \geq H_c$ and by self-organized cell substructures for $H < H_c$.

REFERENCES

1. P. Bak, C. Tang, and K. Wiesenfeld, *Phys. Rev. Lett.*, Vol. 59, 1987, p. 381; *Phys. Rev. A*, Vol. 38, 1988, p. 364.
2. H.J. Jensen, K.C. Christensen, and H.C. Fogedby, *Phys. Rev. B*, Vol 40, 1989, p. 7425.
3. L.P. Kadanoff, S.R. Nagel, L. Wu, and S.-M. Zhou, *Phys. Rev. A*, Vol. 39, 1989, p. 6524.
4. C.P.C. Prado and Z. Olami, *Phys. Rev. A*, Vol. 45, 1992, p. 665.
5. K. Chen, P. Bak, and S.P. Obukhov, *Phys. Rev. A*, Vol. 43, 1991, p. 625.
6. For example, J. Lomnitz-Adler, L. Knopoff, and G. Martinez-Mekler, *Phys. Rev. A*, Vol. 45, 1992, p. 2211; Z. Olami, H.J.S. Feder, and K. Christensen, *Phys. Rev. Lett.*, Vol. 68, 1992, p. 1244; and G. Ekstrom and A.M. Dziewonski, *Nature (London)*, Vol. 332, 1988, p. 319.
7. G.A. Held, D.H. Solina, II, D.T. Keane, W.J. Haag, P.M. Horn, and G. Grinstein, *Phys. Rev. Lett.*, Vol. 65, 1990, p. 1120.
8. H.M. Jaeger, C.-H. Liu, and S.R. Nagel, *Phys. Rev. Lett.*, Vol. 62, 1989, p. 40.
9. K.L. Babcock and R.M. Westervelt, *Phys. Rev. Lett.*, Vol. 64, 1990, p. 2168.
10. H.J.S. Feder and J. Feder, *Phys. Rev. Lett.*, Vol. 66, 1991, p. 2669.
11. P.J. Cote and L.V. Meisel, *Phys. Rev. Lett.*, Vol. 67, 1991, p. 1334.
12. L.V. Meisel and P.J. Cote, *Phys. Rev. B*, Vol. 46, 1992, p. 10822; and *Comp. in Physics*, Vol. 7, 1993, p. 710.
13. J.S. Urbach, R.C. Madison, and J.T. Markert, *Phys. Rev. Lett.*, to be published.
14. C. Kittel, *Elementary Statistical Physics*, Wiley, New York, 1958, pp.153-158.
15. G. Grinstein and S.-K. Ma, *Phys. Rev. B*, Vol. 28, 1983, p. 2599.
16. J. Villain, *Phys. Rev. Lett.*, Vol. 52, 1984, p. 1543.
17. R. Bruinsma and G. Aeppli, *Phys. Rev. Lett.*, Vol. 52, 1984 p. 1547.
18. J. Koplik and H. Levine, *Phys. Rev. B*, Vol. 32, 1985, p.280.

19. T. Natterman, Y. Shapir, and I. Vilfan, *Phys. Rev. B*, Vol. 42, 1990, p. 8577.
20. N. Martys, M. Cieplak, and M.O. Robbins, *Phys. Rev. Lett.*, Vol. 66, 1991, p. 1058.
21. N. Martys, M.O. Robbins, and M. Cieplak, *Phys. Rev. B*, Vol. 44, 1991, p. 12294.
22. D. A. Kessler, H. Levine, and Y. Tu, *Phys. Rev. A*, Vol. 43, 1991, p. 4551.
23. H. Ji and M.O. Robbins, *Phys. Rev. A*, Vol. 44, 1991, p. 2538.
24. B. Koiler, H. Ji, and M.O. Robbins, *Phys. Rev. B*, Vol. 46, 1992, p. 5258.
25. H. Ji and M.O. Robbins, *Phys. Rev. B*, Vol. 46, 1992, p. 14519.
26. O. Narayan and D.S. Fisher, *Phys. Rev. B*, Vol. 48, 1993, p. 7030.
27. B.B. Mandelbrot, *The Fractal Geometry of Nature*, Freeman, New York, 1983.
28. J.A. Nelder and R. Mead, *Computer Journal*, Vol. 7, 1986, p. 308; J.E. Dennis and D.J. Woods, *New Computing Environments: Microcomputers in Large-Scale Computing*, (A. Wouk, Ed.), SIAM, 1987, p. 116.

Table 1. Summary of Fitting Parameters Derived From the Data of Figures 3 Through 9

Two-Dimensional Domain Wall Models (Figures 3 Through 7)							
		Log-Binned Avalanches				Linear-Binned Avalanches	
H	D	C(2)	C(3)	-M	Sharp Cutoff	C(2)	C(3)
200	2.49	0.421	20.7	0.598	30	0.825	11.7
500	2.52	0.269	117	0.340	70	1.065	89.6
700	2.40	0.280	4,191	0.297	2,000	1.290	9,863
1000	2.30	0.322	68,650	0.317	10,000	1.142	27,160
1500	2.30	0.333	∞	0.333	20,000	0.961	21,160
One-Dimensional Domain Wall Models (Figures 8 and 9)							
1000	1.37	0.0556	82.6	0.167	80	0.870	65.8
1500	1.13*	0.107	7,926	0.197	1,100	0.919	3,051
	1.59**						

* 1.13 ($1 \leq Y(m) \leq 16$)

** 1.59 ($16 \leq Y(m) \leq 256$)

Notes: The fractal dimension D is computed from Eq. (4). The fitting parameters C(2) and C(3) are defined in Eq. (5). M is the slope of the sharp cutoff, linear fit to the log-binned avalanche data. The sharp cutoff values for the log-binned data are estimated from the curves in Figures 3 through 9; they are not fitting parameters.

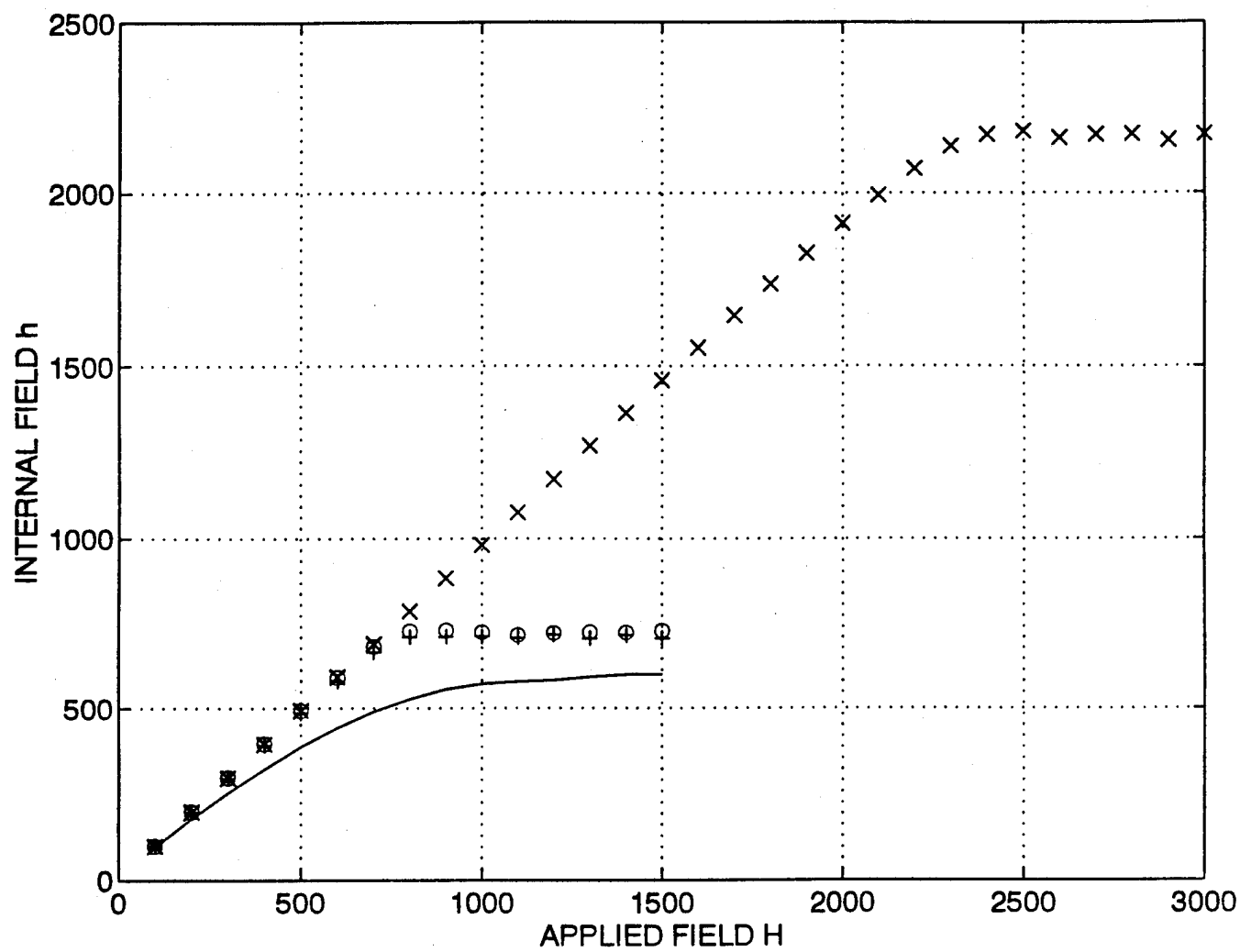


Figure 1. Internal field versus applied field on 65x65 lattices. Legend: x = the {100,1,2000} model; o = the {100,1,1000} model; + = the {100,3,1000} model; Line = the {100,10,1000} model.

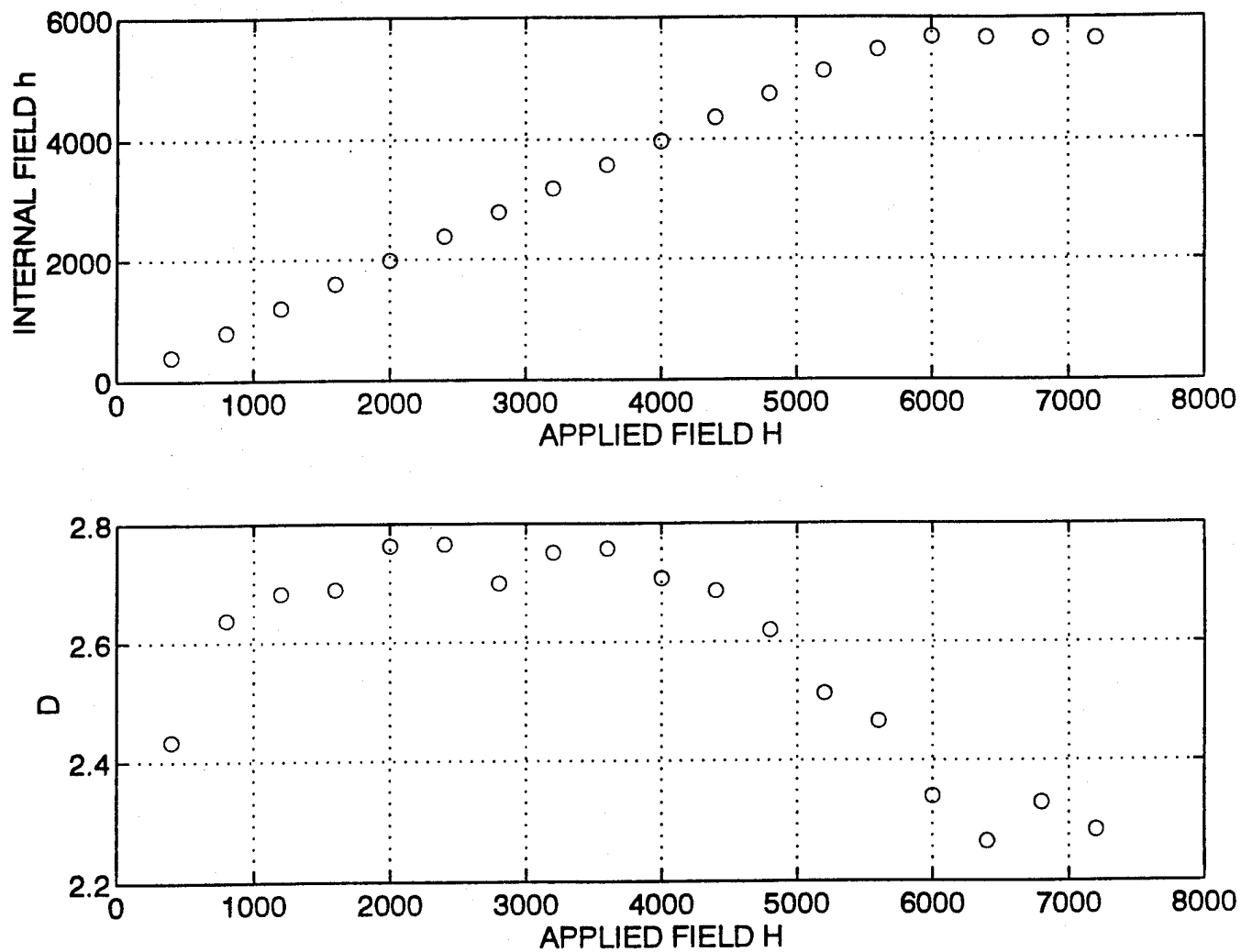


Figure 2. Internal field versus applied field and fractal dimension versus applied field for the {100,10,4000} model on a 65x65 lattice.

NOTES: (1) The upper left-hand subplot shows a contour map of the domain wall displacements for a 65x65 section of the domain wall. There are five equally spaced contour levels. (2) The upper right-hand graph exhibits a graph of $\log_2(A(m)/A(7))$ versus $\log_2(Y(m)/Y(0))$; the straight line is the small yardstick fit. (3) The lower left-hand subplot shows the distribution of avalanche sizes in logarithmically-spaced bins; the straight line is least squares fit to the smaller size half of the distribution; the solid curve is least squares fit to Eq. (5). (4) The lower right-hand subplot shows the distribution of avalanche sizes in linearly-spaced bins; the solid curve is least squares fit to Eq. (5).

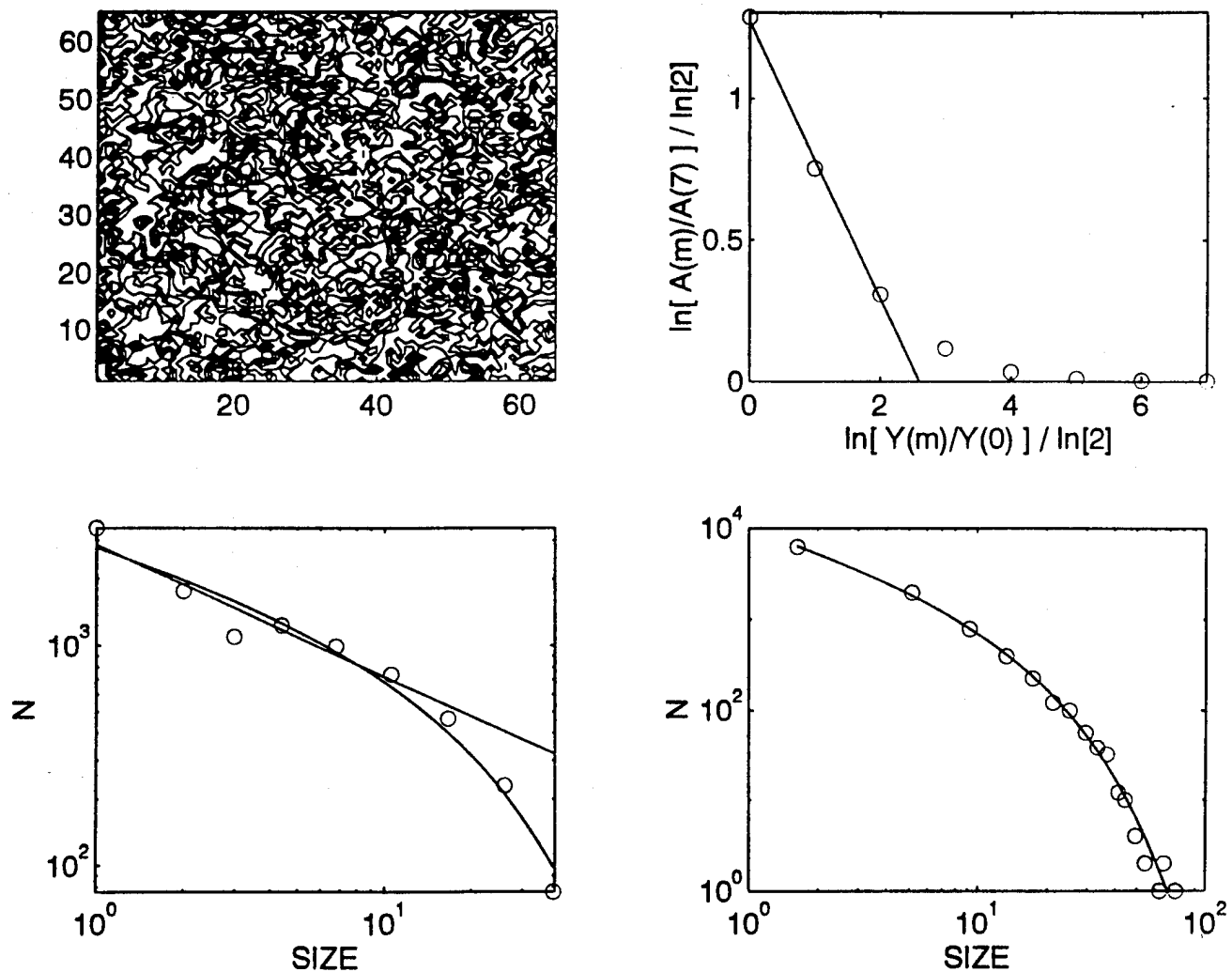


Figure 3. A selection of results for the {100,1,1000} model for $H = 200$ on a 129×129 lattice.

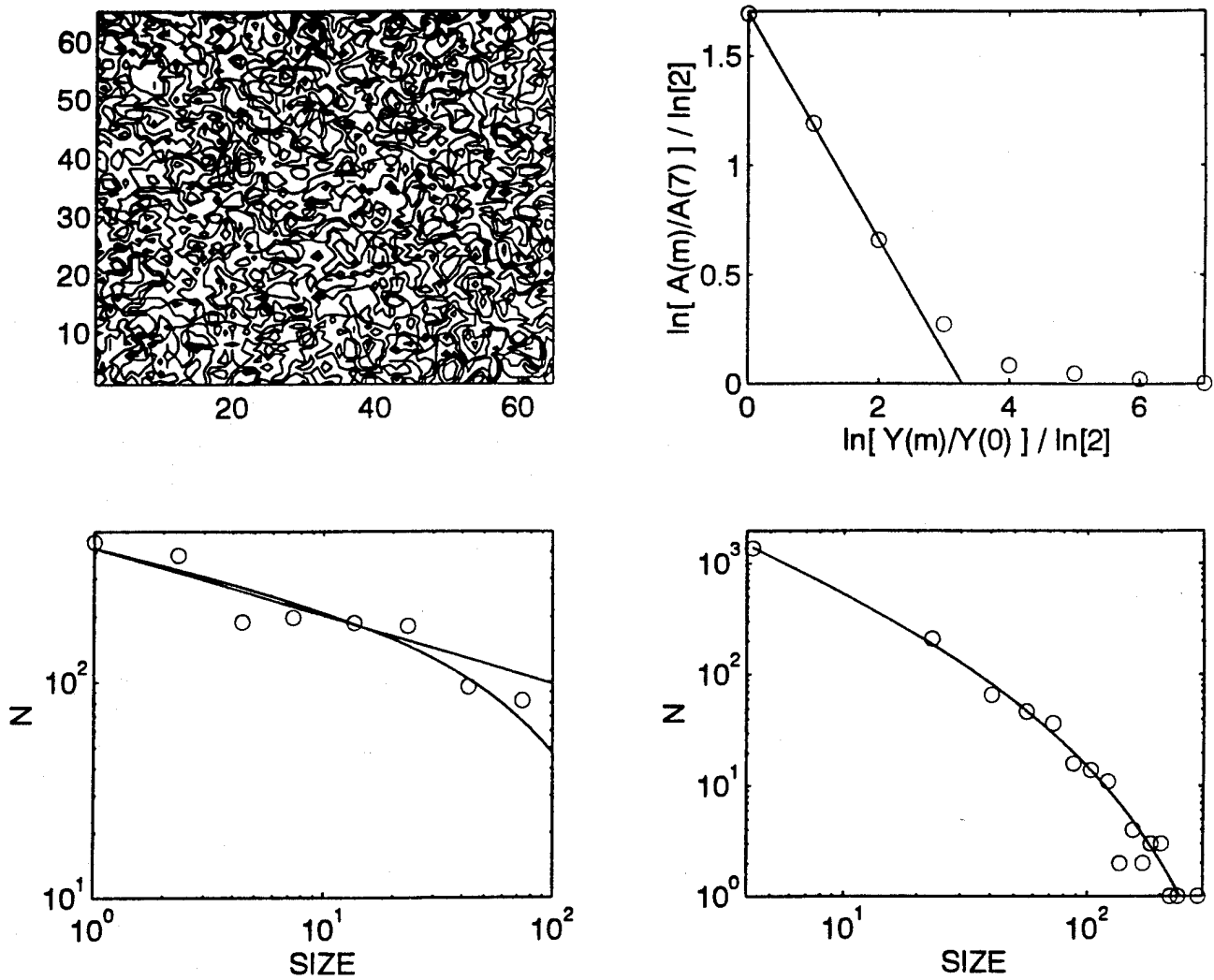


Figure 4. A selection of results for the {100,1,1000} model for $H = 500$ on a 129×129 lattice. The subplots are arranged as in Figure 3.

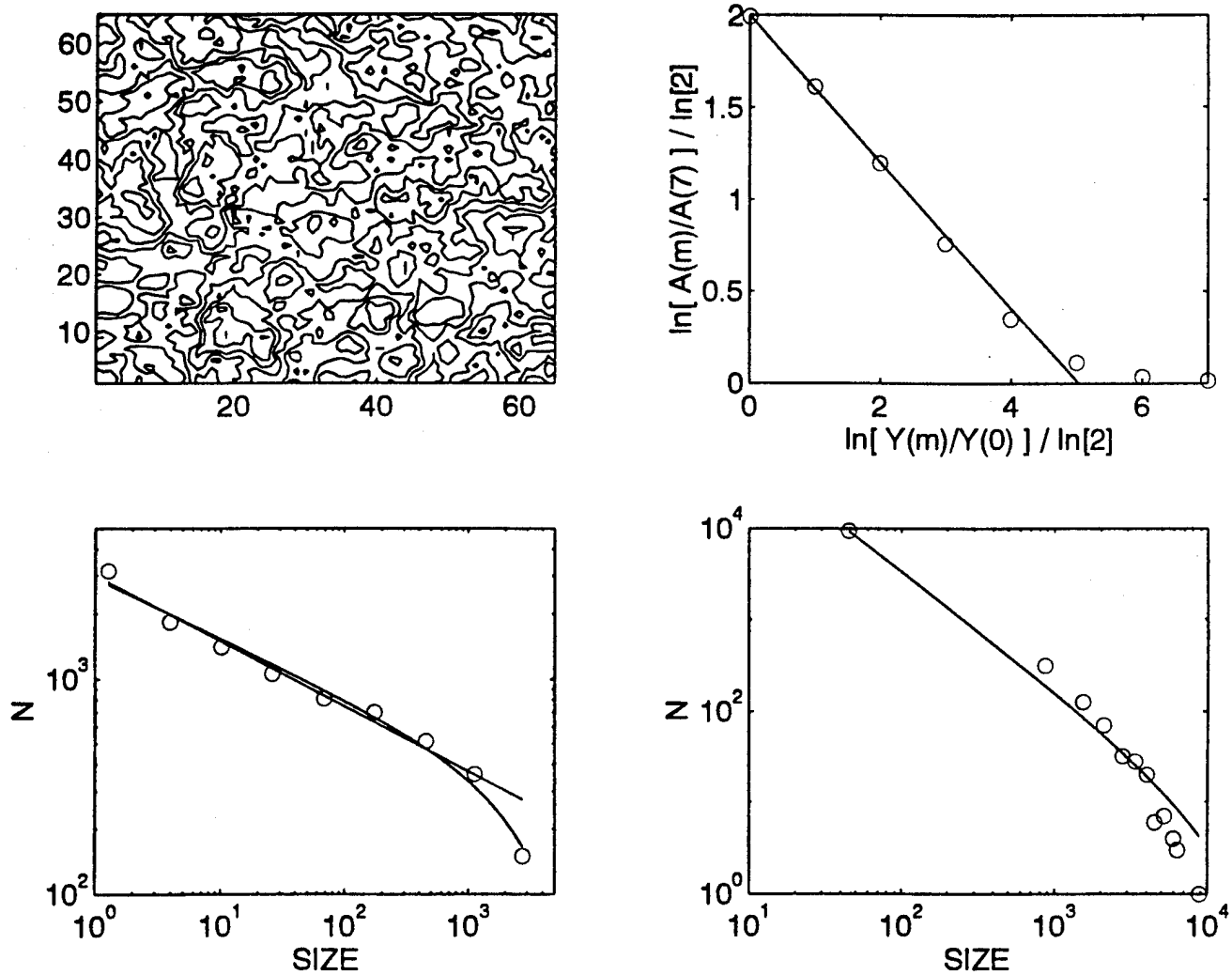


Figure 5. A selection of results for the $\{100,1,1000\}$ model for $H = 700$ on a 129×129 lattice. The subplots are arranged as in Figure 3.

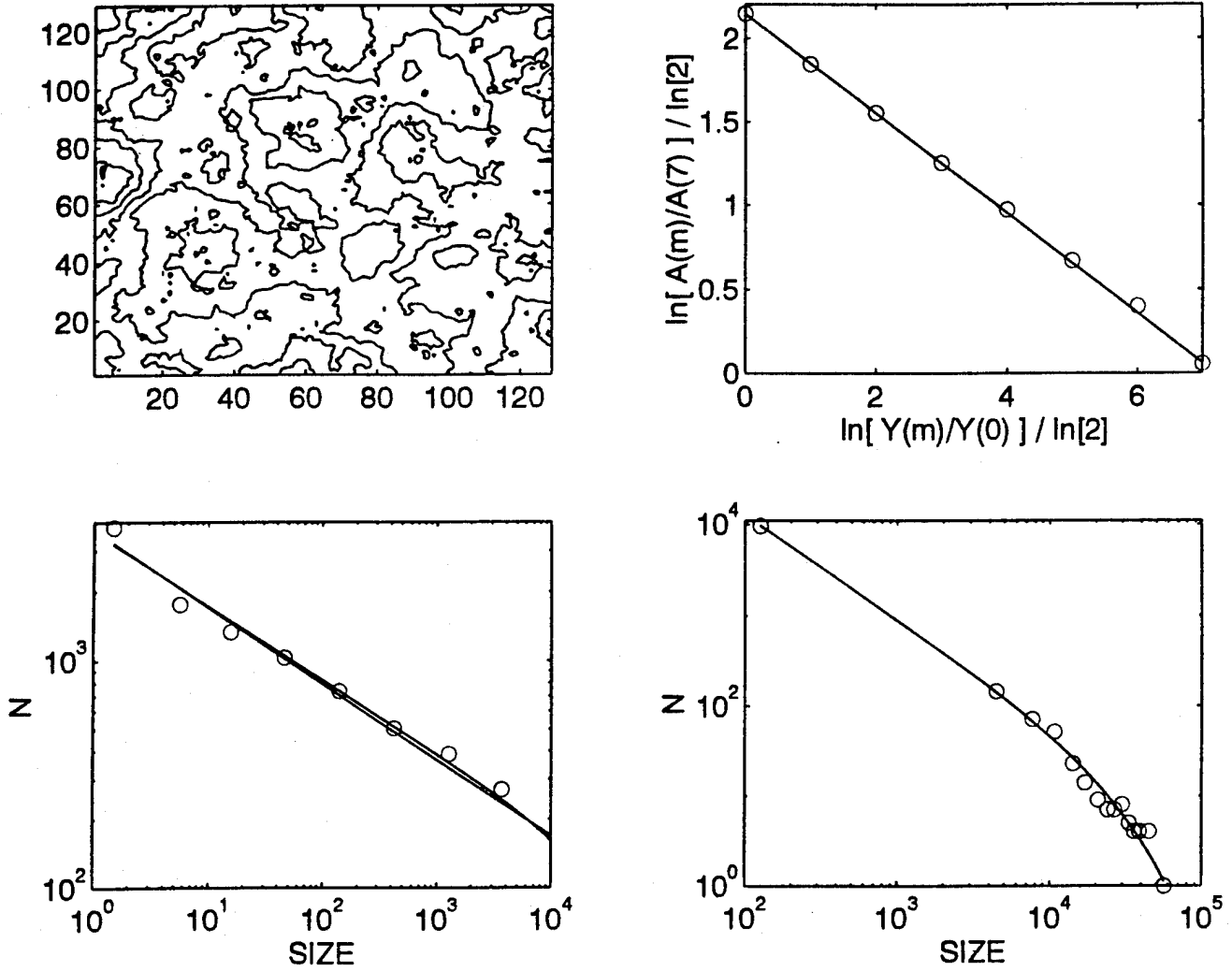


Figure 6. A selection of results for the $\{100,1,1000\}$ model for $H = 1000$ on a 129×129 lattice. The subplots are arranged as in Figure 3, except that the full 129×129 contour plot is shown.

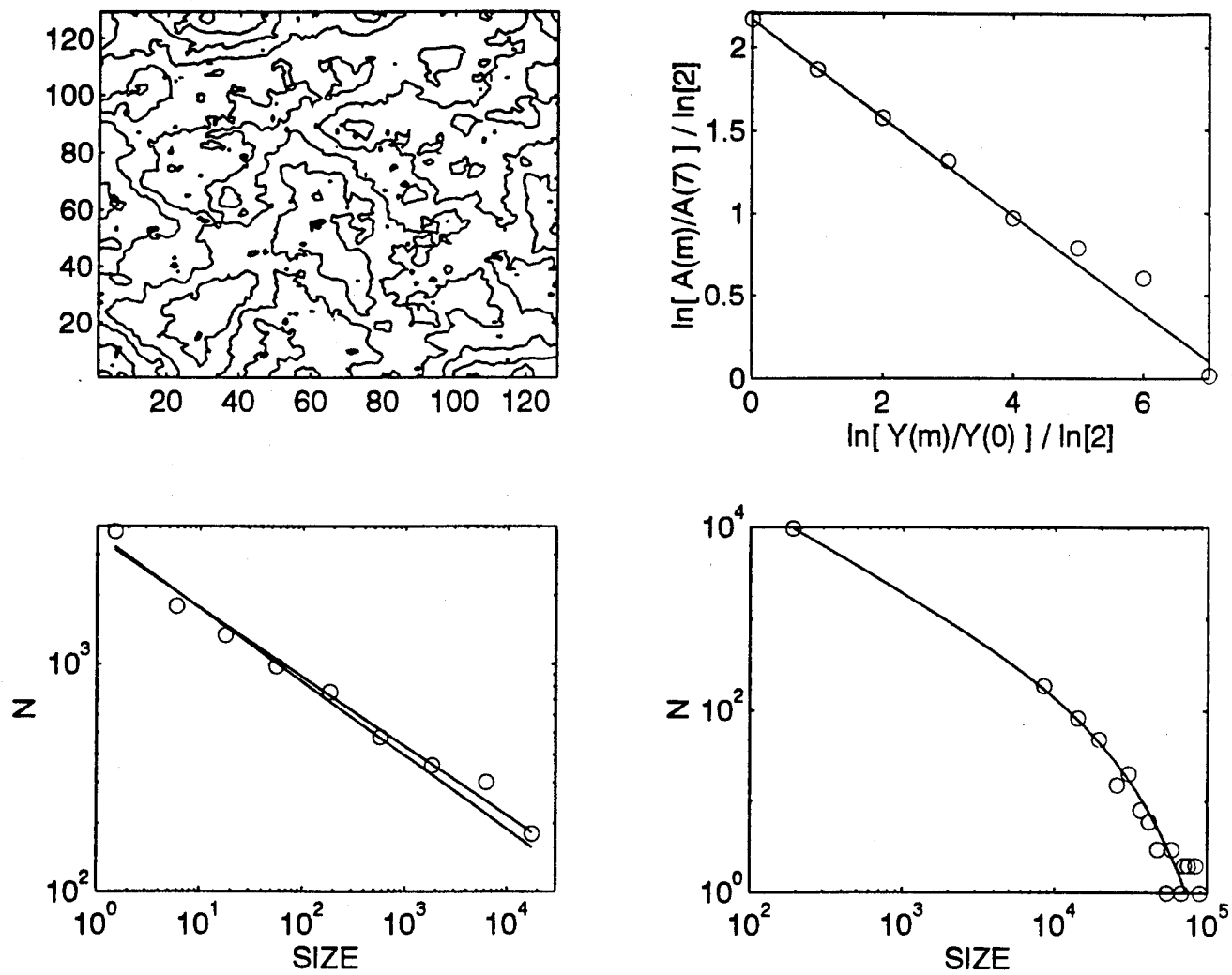


Figure 7. A selection of results for the {100,1,1000} model for $H = 1500$ on a 129×129 lattice. The subplots are arranged as in Figure 6.

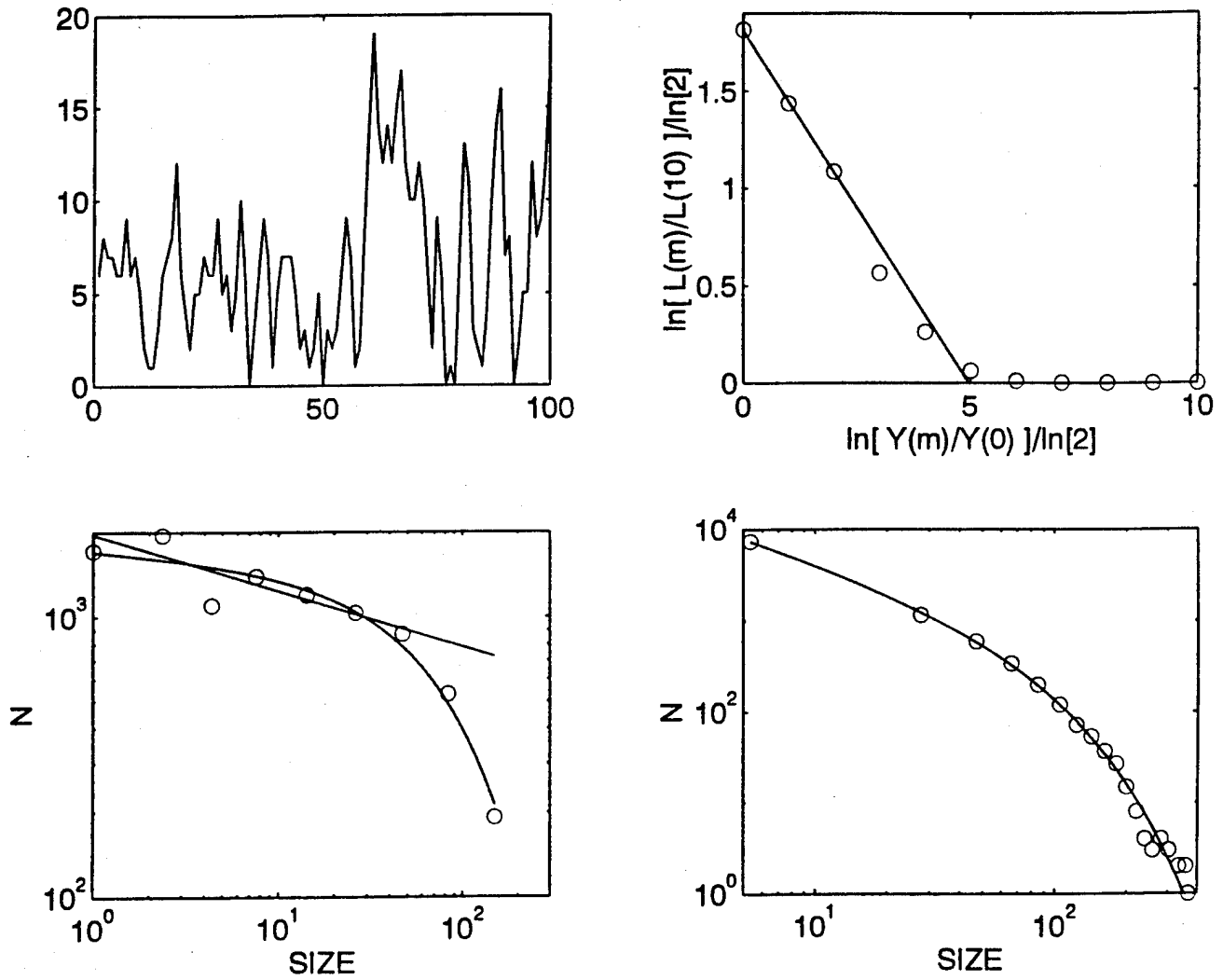


Figure 8. A selection of results for the $\{100,1,1000\}$ model for $H = 1000$ on a 1025 linear lattice. The subplots are arranged as in Figure 3, except that the contour plot is replaced by a displacement plot of a length 100 section of the domain wall and the upper right-hand subplot shows a graph of $\log_2(L(m)/L(10))$ versus $\log_2(Y(m)/Y(0))$ and the small yardstick fit.

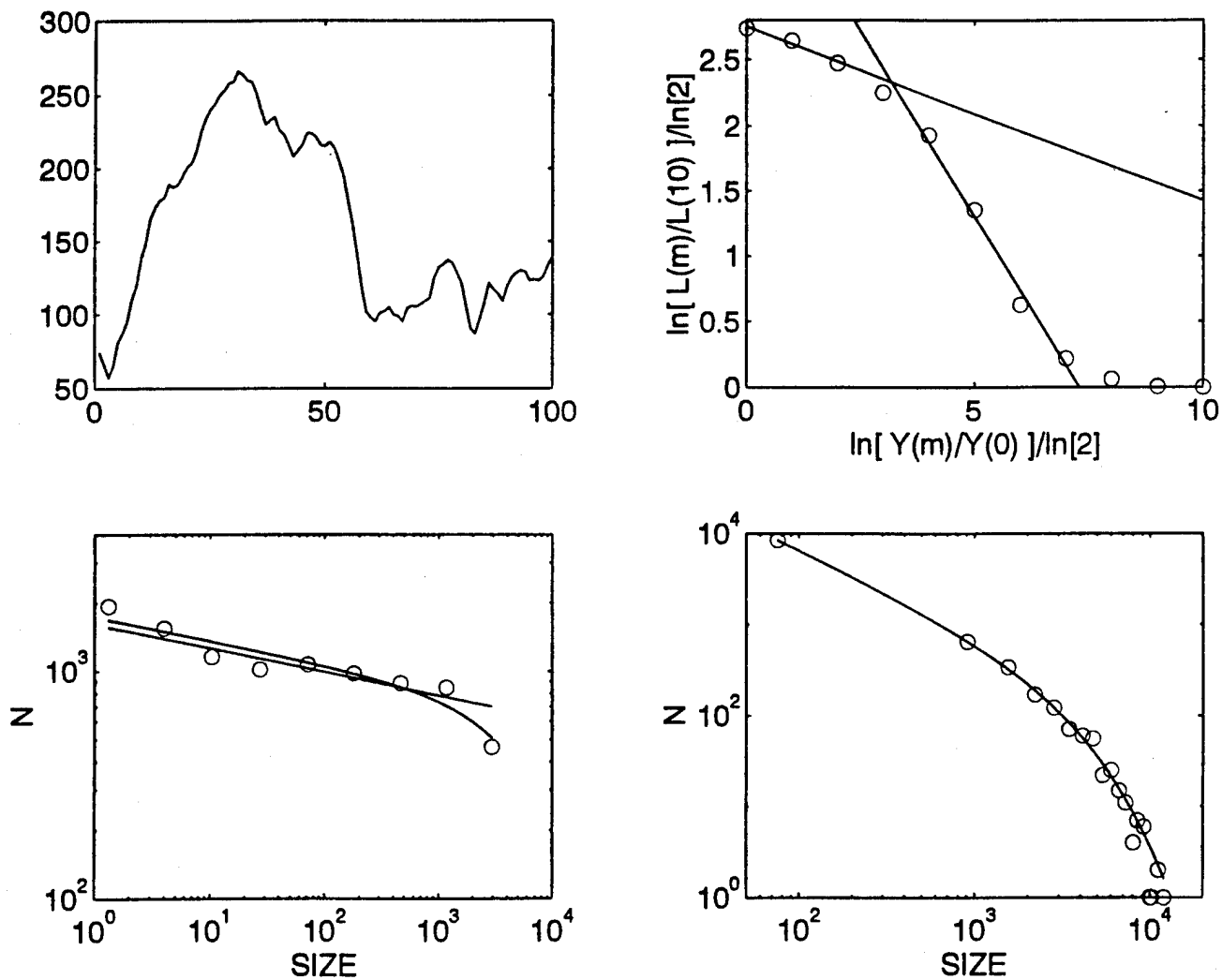


Figure 9. A selection of results for the $\{100,1,1000\}$ model for $H = 150$ on a 1025 linear lattice. The subplots are as those in Figure 8, except that an intermediate yardstick fit is also shown in the upper right-hand panel.

TECHNICAL REPORT INTERNAL DISTRIBUTION LIST

	<u>NO. OF COPIES</u>
CHIEF, DEVELOPMENT ENGINEERING DIVISION	
ATTN: AMSTA-AR-CCB-DA	1
-DB	1
-DC	1
-DD	1
-DE	1
CHIEF, ENGINEERING DIVISION	
ATTN: AMSTA-AR-CCB-E	1
-EA	1
-EB	1
-EC	
CHIEF, TECHNOLOGY DIVISION	
ATTN: AMSTA-AR-CCB-T	2
-TA	1
-TB	1
-TC	1
TECHNICAL LIBRARY	
ATTN: AMSTA-AR-CCB-O	5
TECHNICAL PUBLICATIONS & EDITING SECTION	
ATTN: AMSTA-AR-CCB-O	3
OPERATIONS DIRECTORATE	
ATTN: SMCWV-ODP-P	1
DIRECTOR, PROCUREMENT & CONTRACTING DIRECTORATE	
ATTN: SMCWV-PP	1
DIRECTOR, PRODUCT ASSURANCE & TEST DIRECTORATE	
ATTN: SMCWV-QA	1

NOTE: PLEASE NOTIFY DIRECTOR, BENÉT LABORATORIES, ATTN: AMSTA-AR-CCB-O OF ADDRESS CHANGES.

TECHNICAL REPORT EXTERNAL DISTRIBUTION LIST

	<u>NO. OF COPIES</u>		<u>NO. OF COPIES</u>
ASST SEC OF THE ARMY RESEARCH AND DEVELOPMENT ATTN: DEPT FOR SCI AND TECH THE PENTAGON WASHINGTON, D.C. 20310-0103	1	COMMANDER ROCK ISLAND ARSENAL ATTN: SMCRI-ENM ROCK ISLAND, IL 61299-5000	1
ADMINISTRATOR DEFENSE TECHNICAL INFO CENTER ATTN: DTIC-OCF (ACQUISITION GROUP) BLDG. 5, CAMERON STATION ALEXANDRIA, VA 22304-6145	2	MIAC/CINDAS PURDUE UNIVERSITY P.O. BOX 2634 WEST LAFAYETTE, IN 47906	1
COMMANDER U.S. ARMY ARDEC ATTN: SMCAR-AEE	1	COMMANDER U.S. ARMY TANK-AUTMV R&D COMMAND ATTN: AMSTA-DDL (TECH LIBRARY) WARREN, MI 48397-5000	1
SMCAR-AES, BLDG. 321	1	COMMANDER U.S. MILITARY ACADEMY	
SMCAR-AET-O, BLDG. 351N	1	ATTN: DEPARTMENT OF MECHANICS	1
SMCAR-FSA	1	WEST POINT, NY 10966-1792	
SMCAR-FSM-E	1		
SMCAR-FSS-D, BLDG. 94	1		
SMCAR-IMI-I, (STINFO) BLDG. 59	2	U.S. ARMY MISSILE COMMAND REDSTONE SCIENTIFIC INFO CENTER	2
PICATINNY ARSENAL, NJ 07806-5000		ATTN: DOCUMENTS SECTION, BLDG. 4484 REDSTONE ARSENAL, AL 35898-5241	
DIRECTOR U.S. ARMY RESEARCH LABORATORY ATTN: AMSRL-DD-T, BLDG. 305 ABERDEEN PROVING GROUND, MD 21005-5066	1	COMMANDER U.S. ARMY FOREIGN SCI & TECH CENTER ATTN: DRXST-SD 220 7TH STREET, N.E. CHARLOTTESVILLE, VA 22901	1
DIRECTOR U.S. ARMY RESEARCH LABORATORY ATTN: AMSRL-WT-PD (DR. B. BURNS) ABERDEEN PROVING GROUND, MD 21005-5066	1	COMMANDER U.S. ARMY LABCOM MATERIALS TECHNOLOGY LABORATORY ATTN: SLCMT-IML (TECH LIBRARY) WATERTOWN, MA 02172-0001	2
DIRECTOR U.S. MATERIEL SYSTEMS ANALYSIS ACTV ATTN: AMXSY-MP ABERDEEN PROVING GROUND, MD 21005-5071	1	COMMANDER U.S. ARMY LABCOM, ISA ATTN: SLCIS-IM-TL 2800 POWER MILL ROAD ADELPHI, MD 20783-1145	1

NOTE: PLEASE NOTIFY COMMANDER, ARMAMENT RESEARCH, DEVELOPMENT, AND ENGINEERING CENTER,
BENÉT LABORATORIES, CCAC, U.S. ARMY TANK-AUTOMOTIVE AND ARMAMENTS COMMAND,
AMSTA-AR-CCB-O, WATERVLIET, NY 12189-4050 OF ADDRESS CHANGES.

TECHNICAL REPORT EXTERNAL DISTRIBUTION LIST (CONT'D)

	<u>NO. OF COPIES</u>		<u>NO. OF COPIES</u>
COMMANDER U.S. ARMY RESEARCH OFFICE ATTN: CHIEF, IPO P.O. BOX 12211 RESEARCH TRIANGLE PARK, NC 27709-2211	1	WRIGHT LABORATORY ARMAMENT DIRECTORATE ATTN: WL/MNM EGLIN AFB, FL 32542-6810	1
DIRECTOR U.S. NAVAL RESEARCH LABORATORY ATTN: MATERIALS SCI & TECH DIV CODE 26-27 (DOC LIBRARY) WASHINGTON, D.C. 20375	1 1	WRIGHT LABORATORY ARMAMENT DIRECTORATE ATTN: WL/MNMF EGLIN AFB, FL 32542-6810	1

NOTE: PLEASE NOTIFY COMMANDER, ARMAMENT RESEARCH, DEVELOPMENT, AND ENGINEERING CENTER,
BENÉT LABORATORIES, CCAC, U.S. ARMY TANK-AUTOMOTIVE AND ARMAMENTS COMMAND,
AMSTA-AR-CCB-O, WATERVLIET, NY 12189-4050 OF ADDRESS CHANGES.
